



On the Collisional Disalignment of Dust Grains in Illuminated and Shaded Regions of IC 63

Archana Soam¹ , B.-G. Andersson¹ , Jose Acosta-Pulido² , Manuel Fernández López³ , John E. Vaillancourt⁴ ,
Susanna L. Widicus Weaver⁵, Vilppu Pirola^{6,7} , and Michael S. Gordon¹

¹ SOFIA Science Center, USRA, NASA Ames Research Center, M.S.-12, N232, Moffett Field, CA 94035, USA; asoam@usra.edu

² Instituto de Astrofísica de Canarias (IAC), C/O Via Lactea, s/n E-38205- La Laguna, Tenerife, Spain

³ Instituto Argentino de Radioastronomía (CCT La Plata, CONICET), C.C.5, (1984) Villa Elisa, Buenos Aires, Argentina

⁴ Lincoln Laboratory, Massachusetts Institute of Technology, 244 Wood St., Lexington, MA 02421, USA

⁵ Department of Chemistry, Emory University, Atlanta, GA 30322, USA

⁶ Department of Physics and Astronomy, University of Turku, FI-20014 Turku, Finland

⁷ Finnish Centre for Astronomy with ESO, University of Turku, Turku, Finland

Received 2020 March 27; revised 2020 November 16; accepted 2020 November 16; published 2021 February 2

Abstract

Interstellar dust grain alignment causes polarization from UV to mm wavelengths, allowing the study of the geometry and strength of the magnetic field. Over the last couple of decades, observations and theory have led to the establishment of the radiative alignment torque mechanism as a leading candidate to explain the effect. With a quantitatively well constrained theory, polarization can be used not only to study the interstellar magnetic field, but also the dust and other environmental parameters. Photodissociation regions, with their intense, anisotropic radiation fields, consequent rapid H₂ formation, and high spatial density-contrast provide a rich environment for such studies. Here we discuss an expanded optical, NIR, and mm-wave study of the IC 63 nebula, showing strong H₂ formation-enhanced alignment and the first direct empirical evidence for disalignment due to gas–grain collisions using high-resolution HCO⁺($J = 1-0$) observations. We find that a relative amount of polarization is marginally anticorrelated with column density of HCO⁺. However, separating the lines of sight of optical polarimetry into those behind, or in front of, a dense clump as seen from γ Cas, the distribution separates into two well defined sets, with data corresponding to “shaded” gas having a shallower slope. This is expected if the decrease in polarization is caused by collisions since collisional disalignment rate is proportional to $R_C \propto n\sqrt{T}$. Ratios of the best-fit slopes for the “illuminated” and “shaded” samples of lines of sight agrees, within the uncertainties, with the square root of the two-temperature H₂ excitation in the nebula seen by Thi et al.

Unified Astronomy Thesaurus concepts: [Interstellar dust \(836\)](#); [Polarimetry \(1278\)](#)

1. Introduction

Magnetic fields play a crucial role in the evolution of the interstellar medium (ISM; Crutcher 2004). However, quantitative determinations of the field are notoriously difficult and often very resource intensive to make, such as for Zeeman effect observations (Troland & Crutcher 2008). The easiest observational method for characterizing the magnetic field is via broad-band polarimetry in either the ultraviolet/optical/near infrared (UV/O/NIR) or the far infrared/[sub]mm-wave (FIR/mm). Such polarization is due to dichroic extinction (UV/O/NIR) or emission (FIR) by asymmetric dust grains aligned usually with the magnetic field. To reliably derive magnetic field characteristics from polarization observations, e.g., via “Davis–Chandrasekhar–Fermi analysis” (Davis 1951; Chandrasekhar & Fermi 1953), we must understand the physics of grain alignment in detail. To do so requires a quantitative understanding of the mechanisms both driving and damping the alignment (Draine & Lazarian 1998).

Significant progress has recently been made in the understanding of interstellar grain alignment, both theoretically and observationally. Theoretically, after realizing that paramagnetic relaxation (Davis & Greenstein 1951; Purcell 1979; Mathis 1986) cannot align grains due to internal grain excitation (Lazarian & Draine 1999), a new theory was developed based on radiative drivers (Dolginov & Mitrofanov 1976; Draine & Weingartner 1996; Lazarian & Hoang 2007). Observationally, paramagnetic relaxation alignment was challenged (Jones & Spitzer 1967) by

the finding of grain alignment at large opacities (Jones et al. 1984; Hough et al. 2008). In parallel, the “radiative alignment torque” (RAT) theory has now faced, and met, a number of tests. Andersson & Potter (2007) and Whittet et al. (2008), and recently Medan & Andersson (2019), showed that the alignment is directly correlated with the radiation field strength. Andersson & Potter (2010) showed that the alignment around a localized source (HD 97300, in Chameleon) falls off with distance to the star and that (see Andersson et al. 2011) this alignment varies with the angle between the radiation and the magnetic fields consistent with specific RAT theory predictions. Andersson et al. (2013) have shown that the grain alignment in the reflection nebula IC 63 depends on the H₂ formation rate, again consistent with RAT theory predictions as demonstrated in Hoang et al. (2015). For a recent review of RAT alignment, see Andersson et al. (2015).

Balancing the alignment, several mechanisms might contribute to grain randomization (Draine & Lazarian 1998). For the neutral medium, gas–grain collisions are thought to dominate. In this case, it is easy to show that the characteristic time for the disalignment is given by $t_{\text{random}} \propto (a \cdot n_{\text{gas}} \sqrt{T_{\text{gas}}})^{-1}$ (Whittet 2003), where n_{gas} and T_{gas} are the gas density and temperature and a is the effective grain radius.

We can understand the influence of the driving and damping on the grain alignment through RAT theory. Here we will only sketch a mostly phenomenological approach. We refer the interested reader to Hoang et al. (2015) for a more quantitative analysis. Following Hoang et al. (2015) we can write the

angular momentum (\mathbf{J}) evolution of a dust grain of selected size as the balance between “driving” torques and “damping” by gas–grain collisions and far-infrared emission by the grains:

$$d\mathbf{J}/dt = \mathbf{\Gamma} - C_{\text{coll}}(1 + F_{\text{IR}})n_{\text{H}}\sqrt{T_{\text{gas}}}\mathbf{J} \quad (1)$$

where $\mathbf{\Gamma}$ is the external regular torques on the grain and C_{coll} is a constant for a given grain. The expression $(1 + F_{\text{IR}})$ contains the correction to the angular momentum damping from infrared emission, which, however, is expected to be small for grains larger than $\sim 0.1 \mu\text{m}$ (Draine & Lazarian 1998).

The external torque $\mathbf{\Gamma}$ is made up of a direct RAT component and a H_2 induced torque. These are not fully independent effects in the complex, nonlinear alignment dynamics, where the H_2 torques enhance the radiatively driven torques, lifting grains that would otherwise achieve only poor alignment to efficient alignment at “high- J attractor points” in the dynamical phase-space diagrams (Lazarian & Hoang 2007; Hoang et al. 2015). For simplicity, we will, however, here treat them as separate terms. The radiative torques for grains larger than the minimal available wavelength are proportional to

$$\mathbf{\Gamma}_{\text{rad}} = C_{\text{RAT}}\langle\lambda\rangle u_{\text{rad}} \quad (2)$$

where u_{rad} is the radiation field strength with an average wavelength of $\langle\lambda\rangle$ and C_{RAT} contains both general constants and the geometry—including radiation field anisotropy—of the environment. The H_2 formation torques are given by

$$\mathbf{\Gamma}_{\text{H}_2} = C_{\text{H}_2}\gamma_{\text{H}}n_{\text{H}}(1 - y)\sqrt{T_{\text{gas}}} \quad (3)$$

where γ_{H} is the conversion efficiency from atomic to molecular hydrogen, $y = 2n(\text{H}_2)/n_{\text{H}}$ is the fraction of molecular hydrogen, which is controlled by the radiation field at $\lambda < 1107 \text{ \AA}$ and the self-shielding characteristics of the hydrogen molecule (Federman et al. 1979; van Dishoeck & Black 1986), and we have, similarly to the radiative torques incorporated the H_2 formation parameters (the grain shape, the number of chemisorption sites on the grain, etc.) in the factor C_{H_2} .

In steady state $d\mathbf{J}/dt = 0$ and therefore the maximum angular momentum of the grain in steady state will be (see Hoang et al. 2015):

$$J_{\text{max}} = \frac{C_{\text{H}_2}C_{\text{coll}}}{1 + F_{\text{IR}}}\gamma_{\text{H}}(1 - y) + \frac{C_{\text{RAT}}C_{\text{coll}}}{(1 + F_{\text{IR}})(n_{\text{H}}\sqrt{T_{\text{gas}}})} \quad (4)$$

which, ultimately, controls the polarization efficiency, albeit dependent on a number of complex processes and with several poorly known parameters, such as the grain axis ratio, the amount of super-paramagnetism of the grains, etc. As shown by Hoang et al. (2015), taking the full range of physics into account, ab initio modeling based on RAT theory can reproduce the overall characteristics of the observed polarization in IC 63. We will not, here, try to make such detailed modeling of the alignment, but note that the equilibrium value of J_{max} depends inversely on the gas–grain collision rate.

However, gas–grain collisional damping has, to date, not been directly observationally confirmed (see Andersson & Potter 2007). Here we expand on our earlier results and probe the role of the collisional disalignment. In the present analysis we employ a perturbation-style analysis and will analyze the deviation from the average alignment. That is, as discussed in Section 4, we fit the overall polarization dependence on the H_2

formation rate, find the offsets from this average fit and analyze these differences in the polarization (ΔP) values in terms of the gas density to probe for local, differential collisional effects.

IC 63 is an excellent target for studying radiation driven alignment and collisional disalignment. The region is nearby (at $d \sim 200 \text{ pc}$; van Leeuwen 2007; Andersson et al. 2013) and well characterized with (1) the radiation field from a B0 IV star, $\gamma \text{ Cas}$ (France et al. 2005; Karr et al. 2005), (2) the cloud has been well studied and modeled on global scales (Jansen et al. 1995; Hoang et al. 2015; Andrews et al. 2018), (3) a number of background targets are imaged with polarimetry (Soam et al. 2017) (4) being of limited angular size and relatively dense, molecular rotation lines are used to study spatial variations in collision rates with moderate investments in telescope time. In addition to the generally high densities and temperatures (Jansen et al. 1994), the compression ridge region of the nebula shows additional enhancements in both, with density $n = 10^5\text{--}10^6 \text{ cm}^{-3}$ (Polehampton et al. 2005), and temperature $T \sim 600 \text{ K}$ (Fleming et al. 2010).

The IC 63 cloud has been studied in O/NIR polarimetry by Andersson et al. (2013) and Soam et al. (2017). The former used optical polarimetry combined with NIR observations of the fluorescence in the 1-0 S(1) line of H_2 to show that the grain alignment is enhanced by the formation torques of the ejection from newly formed H_2 molecules. Hoang et al. (2015) used ab initio modeling based on RAT theory to reproduce the grain alignment in the different parts of the cloud, taking into account both the direct radiative torques and the torques from H_2 formation. In both studies outliers exist at anomalously low values of the measured polarization.

In addition to finding H_2 formation driven grain alignment in parts of IC 63, Andersson et al. (2013) also found anomalously inefficient alignment in the compression ridge region as well as a much steeper fall-off in the fractional polarization (P/A_{V}) with column density ($P/A_{\text{V}} \propto A^{-1.1 \pm 0.1}$) than in the general ISM ($P/A_{\text{V}} \propto A^{-0.52 \pm 0.07}$); Whittet et al. 2008). A power-law exponent of -1 indicates that the alignment is generated only in a surface layer of the nebula. Based on the studies by Jansen et al. (1994), Polehampton et al. (2005) and Fleming et al. (2010), the rapid loss of alignment with A_{V} and the high contrast in density between the compression ridge and cloud in the IC 63 could likely point to collisional disalignment as a cause of the outliers.

In this work, we have acquired additional polarimetric measurement of the nebula as well as high-resolution mapping in the HCO^+ ($J = 1\text{--}0$) line, which allow us to address the effects of gas–grain collisions on the grain alignment. The HCO^+ ($J = 1\text{--}0$) line intensity is a sensitive indicator of the gas column density, but only slowly varying functions of temperature (Jansen et al. 1994). The detailed modeling of Jansen et al. shows that IC 63 is an optically thin ($\tau \sim 0.1$) region due to its relatively warm ($\sim 100 \text{ K}$) nature.

The paper is organized as follows: in Section 2, we describe the observations and data reduction; in Sections 3–5, we describe, discuss and summarize our results of this work.

2. Observations

2.1. Archival Data

We used our existing optical and NIR polarimetric observations from Andersson et al. (2013) and Soam et al. (2017). Optical polarization observations toward 12 stars were made at the Nordic Optical Telescope (NOT) on La Palma

using ALFOSC and TURPOL instruments in spectropolarimetry and photopolarimetry modes, respectively. The details of the observations are given in Andersson et al. (2013).

For correlating the polarization fraction with grain alignment caused by *Purcell mechanism* (Purcell 1979), we used the H₂ 1-0 S(1) observations from Andersson et al. (2013). These deep narrow-band imaging observations at 2.122 μm were acquired with the WIRCam instrument (Puget et al. 2004) at the Canada–France–Hawaii Telescope (CFHT). To better analyze the diffuse emission, we had to first perform a star subtraction of the foreground sources. We used the Astropy-affiliated photutils (Bradley et al. 2019) package to construct an effective point-spread function (ePSF) from stars extracted over the entire image. Combined with two-dimensional background estimation and modeling, the ePSF was used to subtract away point sources, leaving the underlying diffuse emission intact.

2.2. Optical Spectropolarimetry

Additional optical spectropolarimetric observations were acquired on 2013 October 18 and 19 from the Intermediate-dispersion Spectrograph and Imaging System (ISIS) mounted at the $\sim f/11$ Cassegrain focus of the 4.2 m William Herschel Telescope (WHT) in the Canary Islands, Spain. Observations were acquired with both the red and blue sides of the spectrograph. For the blue arm we used the EEV12 CCD providing good quantum efficiency down to the atmospheric cut-off and the R300B grating centered at 4500 Å. For the red arm we used the Red+ CCD and the R158R grating centered at 6400 Å. The blue observations were corrupted by scattered light and are not discussed here. The red data cover $\lambda \approx 0.48\text{--}0.95 \mu\text{m}$. For comparison with earlier data we have extracted the polarization values at 0.65 μm . HD 204827 was used as the high-polarization standard and HD 212311 was observed as a zero-polarization standard. We divided the total integration time into eight half-wave plate (HWP) settings, to minimize the influence of systematic errors. Data reduction was accomplished through standard IRAF routines.

2.3. HCO⁺ Line

Observations of the $J = 1\text{--}0$ line of HCO⁺ at 89.189 GHz were conducted using the Combined Array for Research in Millimeter-wave Astronomy (CARMA) in the 15-element mode (six 10.4 m antennas and nine 6.1 m antennas). Observations were conducted in three tracks separated by a few days (2014 February 13, 14 and 17), with CARMA in its C configuration (baselines ranging 30–350 m). A six pointing mosaic with the phase center aiming at $\alpha_{J2000} = 00^{\text{h}}59^{\text{m}}01.22^{\text{s}}$ and $\delta_{J2000} = +60^{\circ}53'23''.40$ was implemented. Good atmospheric conditions prevailed for the observations with an average opacity at 230 GHz between 0.15 and 0.3 for the three tracks. The total time on source was 9.4 hr.

The first local oscillator (LO) was set to 91.0163 GHz (3.3 mm). The correlator configuration provided simultaneous observations of the continuum emission (1.9 GHz of total bandwidth) and several lines, including HCO⁺ (1-0) and HCN (1-0) among others. Here we present the HCO⁺ (1-0) data (rest frequency 89.18853 GHz), which lay in one of the ten spectral windows each consisting of 159 channels with 50 KHz each (i.e., 0.16 km s^{−1} at the observing frequency) and 8 MHz total width (about 26 km s^{−1}).

The data were edited, calibrated, and imaged using the MIRIAD package (Sault & Noordam 1995) in a standard way. Quasars 3C84 and J0102+584 were used as bandpass and phase calibrator, respectively. Observations of Uranus provided the absolute scale for the flux calibration of the data set. The measured flux of J0102+584 was 2.6 Jy and the flux uncertainty for CARMA observations at 3 mm is estimated to be 10%.

A continuum image was created by combining the data set of the three tracks using the Miriad program INVERT with a natural robust weighting. The rms noise of the resulting interferometer-only image has a synthesized beam of $5''.9 \times 4''.9$ with a P.A. of 48° and an rms noise level of 0.3 mJy beam^{−1}. No continuum emission is detected over a 3σ level. The HCO⁺ (1-0) line image was created using a natural weighting scheme too and the interferometer-only velocity cube has a synthesized beam of $6''.1 \times 4''.7$ with a P.A. of 57° and an rms noise level of 97 mJy beam^{−1}.

Single dish observations covering the IC 63 interferometry pointings were also acquired with the EMIR instrument on the IRAM 30 m telescope during 2013 July 21–23. The observations were carried out in on-the-fly (OTF) mapping, position-switching mode, using a velocity resolution of 0.13 km s^{−1}. The final map covering $4''.0 \times 2''.8$ was obtained.

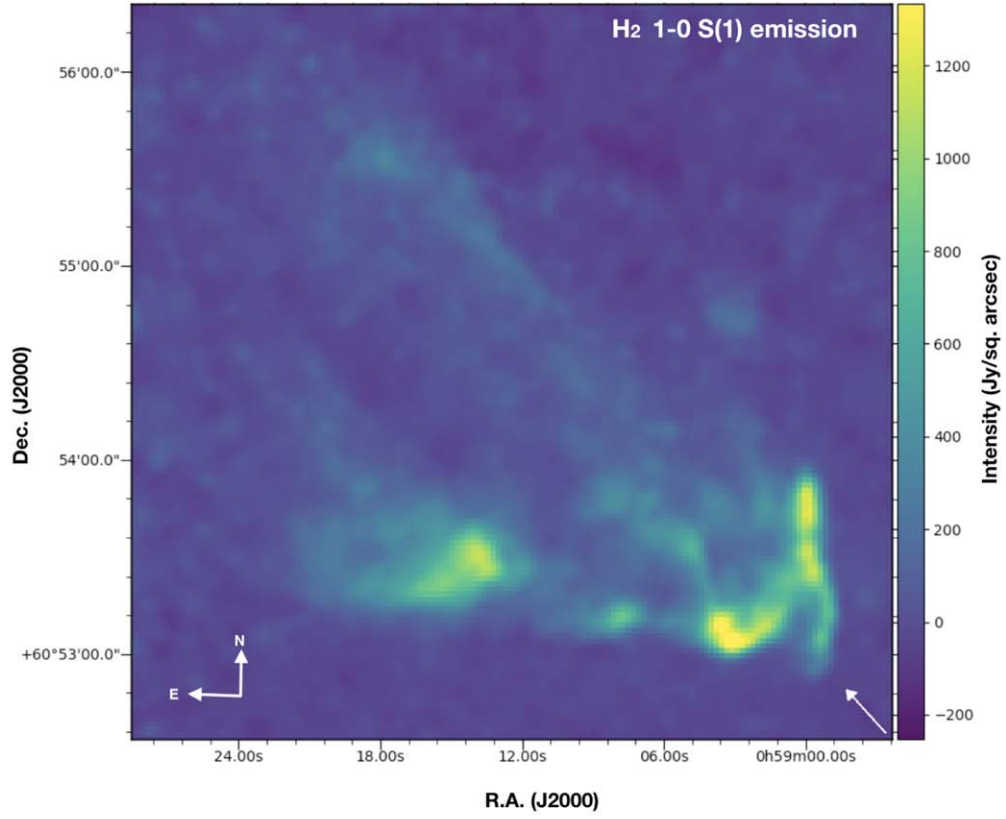
After calibrating the CARMA interferometer visibilities, we combined the HCO⁺ (1-0) with a map taken with IRAM 30 m. For this purpose we created an interferometer image using a robust weighting of 0.5 and converted the IRAM 30 m Dish data to Jy beam^{−1} using a Jy-per-K factor of 6.0⁸ for observations at 86 GHz. We made a jointly–deconvolution of the interferometer and the single-dish data sets using the Miriad program MOSMEM and then restoring the resulting image with a synthesized beam of $5''.8 \times 4''.4$ with a P.A. of 50°. The final image has an rms noise level of 6 mJy beam^{−1}. Finally, we also made a HCO⁺ (1-0) integrated intensity image, collapsing the emission from -0.9 to 1.5 km s^{−1}. This image has an rms noise level of about 24 mJy beam^{−1} km s^{−1}.

3. Results

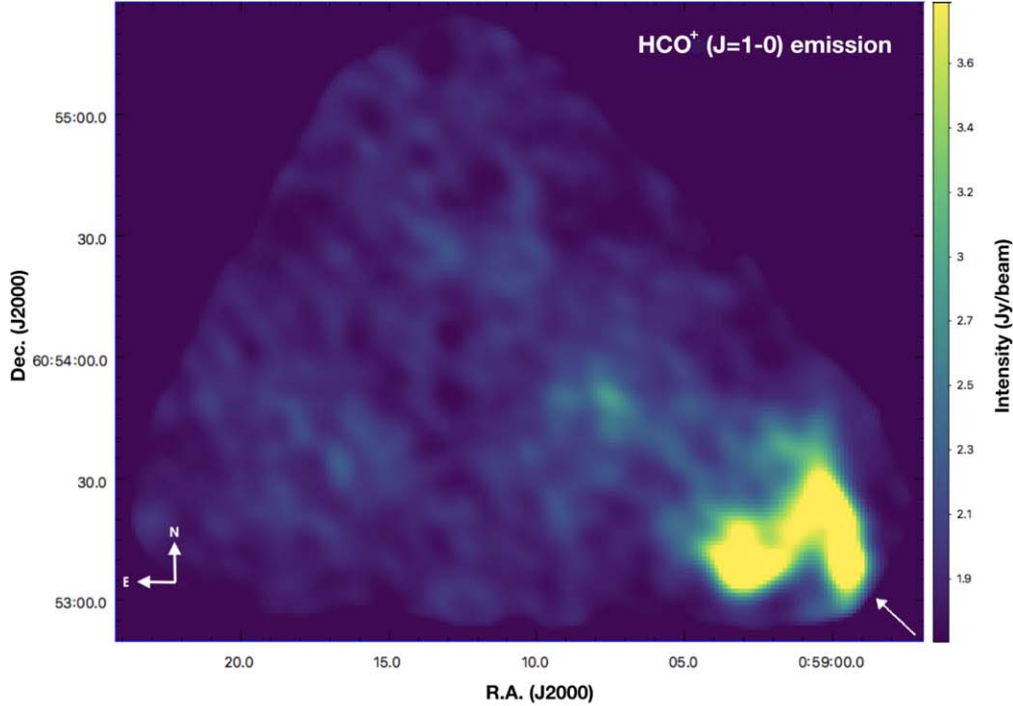
Figure 1 shows emission maps of $\nu = 1\text{--}0$ H₂ $J = 1\text{--}0$ (upper panel) and HCO⁺ $J = 1\text{--}0$ (lower panel) toward IC 63. The clumpiness in H₂ emission with a hook-like emission feature can be clearly seen. Also, the HCO⁺ gas is mostly localized in the front of the nebula looking toward high energy radiation from γ Cas (as seen in the PdBI data from Polehampton et al. 2005). The hook-like feature is common in both emission maps indicating the gaseous evaporation on the side facing the ionizing radiation (Caputo et al. 2021). The directions of ionizing radiations (i.e., from southwest to northeast) are shown using white arrows in both panels.

Thi et al. (2009) observed the lowest pure-rotational lines S(0); $J = 2\text{--}0$, S(1); $J = 3\text{--}1$, S(3); $J = 5\text{--}3$ and S(5); $J = 7\text{--}5$ of H₂ toward IC 63 using the Short Wavelength Spectrometer (SWS) of the Infrared Space Observatory (ISO). The apertures of the SWS are fairly large on the scale of the H₂ ridge ($20 \times 27''$ at S(0), $14 \times 27''$ S(1), and $14 \times 20''$ at the S(3) and S(5) lines) and the emission may therefore probe several different physical regions. Figure 2 shows their H₂ excitation diagram toward the IC 63 PDR and illustrates that the observed intensities are best fit with two thermal components with $T = 106 \pm 11$ and 685 ± 68 K, respectively. Thi et al. (2009)

⁸ http://www.iram.es/IRAMES/telescope/telescopeSummary/telescope_summary.html



(a)



(b)

Figure 1. Upper and lower panels show the H_2 and HCO^+ gas emission maps toward IC 63 nebula, respectively. The interesting *hook-like* feature can be seen in both images toward the region facing ionizing radiation. The directions of radiation are shown with a thick arrow in both the panels.

compared their observations with available photochemical models (Thi et al. 1997; Kaufman et al. 1999; Röllig et al. 2007) based on optical absorption and/or millimeter emission

data with and without enhanced H_2 formation rate on grain surfaces. The inferred column densities of these two regions are $(5.9 \pm 1.8)^{+0.9}_{-0.7} \times 10^{21} \text{ cm}^{-2}$ and $(1.2 \pm 0.4) \times 10^{19} \text{ cm}^{-2}$,

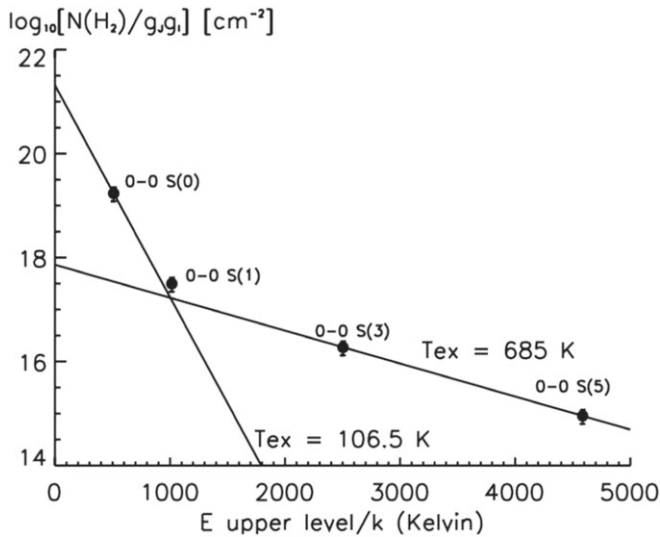


Figure 2. The H_2 excitation diagram toward the IC 63 PDR derived from the ISO-SWS observations. This plot is adopted from Thi et al. (2009).

corresponding to the warm and hot components, respectively. The ISO temperature estimate of the hot region (Thi et al. 2009) is consistent with the ISOCAM results (630 K) of Karr et al. (2005) and the Spitzer/IRS results of Fleming et al. (2010). Because Fleming et al. (2010) did not have access to the long wavelength spectra from Spitzer IRS-LL for IC 63, they were not able to probe the presence or distribution of the warm (~ 100 K) gas.

In Figure 3, we show the spatial locations of the stars plotted on clumpy HCO^+ emission toward IC 63 (this figure is deliberately stretched to see the clumpy structures). The polarization observations of these stars are available in Andersson et al. (2013) and Soam et al. (2017). The stars are either located, in projection, behind (blue dots) or in front (red dots) of the clumpy structures of HCO^+ emission. The true, physical, distances of these stars toward IC 63 are irrelevant as long as we assume that the IC 63 cloud is the only layer of dust by which the background starlight is polarized along the line-of-sight (Soam et al. 2021). We are only concerned with the locations in the nebulae where the light is shining through the cloud and getting polarized, either in front of or behind the HCO^+ clumps. So the contributions of clumps of the nebulae in polarizing the light are more important than the actual distances of the sources of the light (i.e., background stars). The cartoon shown in Figure 4 illustrates this by showing the locations of the main cloud IC 63 (assuming a slab-like geometry), ionizing source with a blue star symbol, and stars behind the cloud shown with yellow star symbols. The HCO^+ clump is shown as a shaded cuboid symbol with its front and behind lines of sight through the cloud shown as red and blue line-segments. The polarized light from these front and behind the clump lines of sight is measured. These HCO^+ clumps represent the gas densities, and the variation of any change in polarization may be due to the dust [in the cloud] and gas collisions.

Figure 5 shows the variation of polarization fraction (data included both from Andersson et al. 2013 and Soam et al. 2017) with the H_2 intensities at the locations of nebula where polarization is detected. This variation is fit by using linear regression and robust linear model fits to these data. The upper panel shows the result of the Robust linear model fit. This model is less sensitive to the outliers. The lower panel shows the linear

regression fit. Both the models show data fit differently but the output fit value of P is almost the same (i.e., $\sim 3.5\%$).

Figure 6 shows the variation of difference in polarization fraction (ΔP) with HCO^+ intensities at the locations of the stars shown in Figure 3.⁹ We denote ΔP as the difference in observed amount of polarization and best-fit value of polarization ($\Delta P = P - P_{\text{fit}}$) obtained from Figure 5, as ΔP in this plot. The color of the symbols (red and blue) in Figure 6 are deliberately chosen to connect this figure with locations of stars shown in Figure 3. The white dots in Figure 3 are those which are neither exactly behind nor in front of the clumps. We plotted their values with red points in Figure 6.

4. Discussion

4.1. Grain Alignment with Purcell Torques

Purcell (1979) proposed three surface processes to drive grains to suprathermal rotation. Among these three processes, the formation of H_2 molecule at the catalytic site was suggested as the dominant mechanism to produce rotational torques. In addition to the work of Purcell (1979), Lazarian & Draine (1997), and Lazarian & Roberge (1997) presented the detailed calculations for these torques for a brick-like and a spheroidal grain. As noted by Andersson et al. (2013), if the H_2 emission from a region is fluorescent in origin, then the intensity of the emission traces the molecular hydrogen formation rate. This is because H_2 photo destruction proceeds via a two-step process initiated by a line absorption in the Lyman or Werner bands, followed by a relaxation of the electronic excitation. The direct photodissociation of an H_2 molecule requires a photon with energy $E > 14.7$ eV (Stecher & Williams 1967), well above the ionization energy of atomic hydrogen ($E = 13.6$ eV) and is thus not important in the atomic ISM. During the relaxation process, the molecule dissociates if the vibrational state of the de-excited molecule has $v > 14$. If it re-enters the electronic ground state at a lower vibrational quantum number, the molecule will proceed to the ground state through a rotational-vibrational cascade observable chiefly in the NIR. Since the branching ratio between dissociation and fluorescence cascade is determined by quantum mechanics, the fluorescence rate is directly proportional to the molecular destruction rate. As the dynamical timescales in a well-established PDR are much longer than those of molecular formation and destruction (Tielens 2005; Morata & Herbst 2008), the abundance of H_2 is governed by a detailed balance equation where formation and destruction rates equal each other. The fluorescent intensities, therefore, trace the formation rate of the molecule.

The formation of molecular hydrogen on the surface of the dust grains helps in spinning up the grains (Purcell 1979). When the molecule leaves the grain surface, it imparts a net torque to the dust grain which results in spinning of the grain. This phenomena is called the “Purcell rocket effect.” These torques cause the grains to rotate suprathermally (i.e., with rotational energies well above the thermal energies of the gas or dust). These spinning grains interact with interstellar magnetic fields and become aligned with the field with spinning axes parallel to the field orientation. These “Purcell torques” play an important role also in modern RAT based grain alignment,

⁹ The number of blue data points in Figure 3 are six but there are five blue data points shown in Figure 6. This is because we dropped one star which has unusually high ΔP and large uncertainty in polarization measurement. There are fourteen red points in Figure 6 but only twelve in Figure 3. We considered two extra stars from Soam et al. (2017) with those from Andersson et al. (2013).

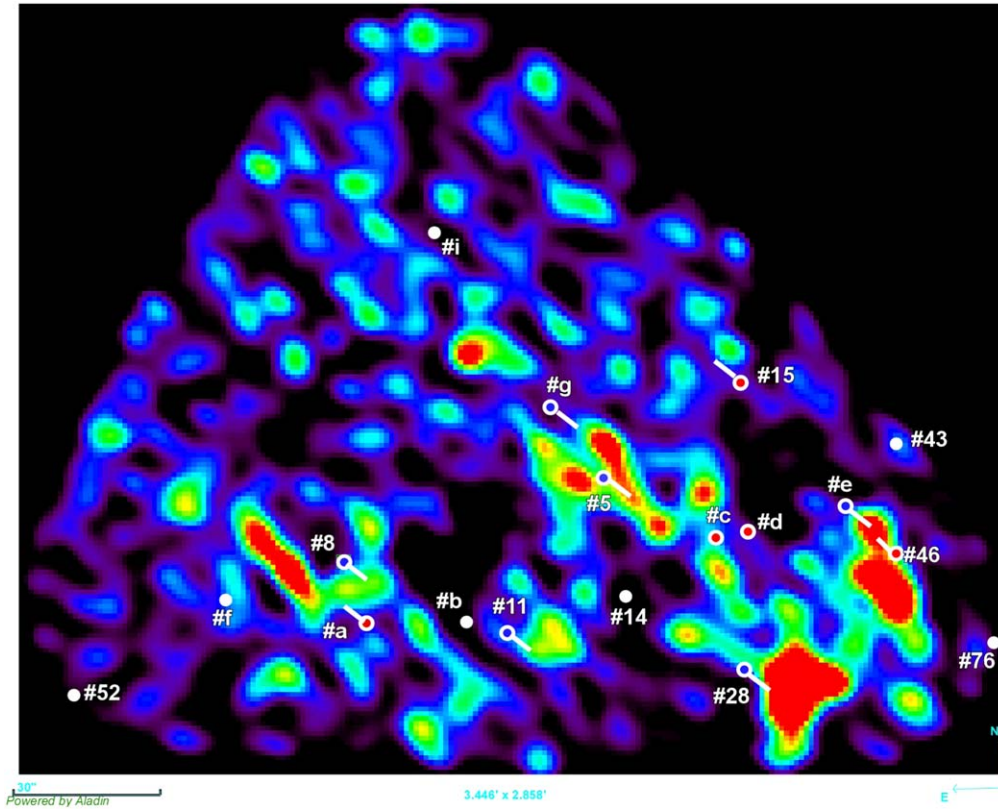


Figure 3. The location of stars with optical polarization observations shown on the $\text{HCO}^+(J = 1-0)$ map. Stars behind the clumps and in front of the clumps are shown with blue and red colors, respectively. A number of lines of sight do not clearly fall in either category. These are plotted as white symbols.

where they enhance the radiatively driven alignment allowing a larger fraction of the grains to attain suprathermal rotation.

Andersson et al. (2013), using their spectropolarimetric observation with NOT/ALFOSC and five-band photopolarimetry with NOT/TURPOL for stars toward IC 63, studied the correlation between polarization and diffuse H_2 fluorescence emission in the cloud. They note that the polarization seen in IC 63 is proportional to the level of H_2 fluorescence (i.e., H_2 formation rate) for high intensity H_2 emission fluorescence (i.e. $I_{\text{H}_2} > 10^{-5} \text{ erg cm}^{-2} \text{ s}^{-1} \text{ sr}^{-1}$). They identified this correlation as the signature of enhanced dust grain alignment driven by H_2 formation. No clear correlation was seen for $I_{\text{H}_2} < 10^{-5} \text{ erg cm}^{-2} \text{ s}^{-1} \text{ sr}^{-1}$ suggesting that up to this formation rate, only direct RAT alignment dominates. They also note a few outliers. We have used their polarization measurements in addition to values from Soam et al. (2017) to re-investigate the relation between amount of polarization increment with H_2 formation on dust grains (see Figure 5). The star numbered 46 (see Figure 3) is in common in the two studies. For this particular star, we use the polarization values from Soam et al. (2017).¹⁰

¹⁰ The sky subtraction process of Soam et al. (2017) was better for star #46 as they used CCD-based imaging polarimetry, while TURPOL is a two-channel photopolarimeter with a fixed sky aperture. Soam et al. (2017) used the FITSKYPARS task in the IRAF apphot package to subtract the sky background. An aperture is created centered on the star with a radius of twice the FWHM of the Gaussian distribution of the star counts. A sky annulus is created around the star and background contribution is measured within this annulus. The size of the annulus was chosen to yield approximately constant background counts (i.e., avoiding the extended stellar PSF). This value is subtracted from the signal within the aperture. Because of the offset sky aperture, there are chances of diffused emission contamination in the result of Andersson et al. (2013). They discuss the background contamination in the TURPOL observations in Appendix A.2.

The polarization results from Soam et al. (2017) and Andersson et al. (2013) are consistent within the uncertainties.

Panel (a) of Figure 5 shows robust linear model (RLM) fitting in distribution of amount of polarization we have from observations and the intensity of H_2 fluorescence measured at the same locations where we detected polarization. Panel (b) also shows the distribution of same quantities but with linear regression model (LM) fit to the data and uncertainty in the fit model is shown with shaded blue region. These two different models have different functions when fit to the data. LM is just ordinary least square fitting which reduces the residuals, whereas in RLM, all data points are not treated equally. Robust fitting is not sensitive to outliers but LM is very sensitive to the outlying data points. If the uncertainties are of a fully random nature LM is the more appropriate technique. However, RLM fitting is useful for samples where additional unaccounted for parameters may be producing significant systematic errors in the data. The distribution shown in Figure 5 is quite scattered. Therefore, we used both RLM and LM methods. In both the panels, a trend of increase in polarization with intensity of H_2 fluorescence can be noticed. The correlation is not as good as seen by Andersson et al. (2013) who had a lesser number of targets. Although more data should nominally improve the sampling of an underlying relationship, this is only true if the noise in the data set is statistical/random in nature. If the noise is instead systematic, more sampling may not yield tighter correlations. Because of the good correlation seen in Andersson et al. (2013), the formal correlation seen in this larger sample and the highly successful ab initio modeling of the alignment in this [physically simple] system by Hoang et al. (2015), we feel justified in probing for a

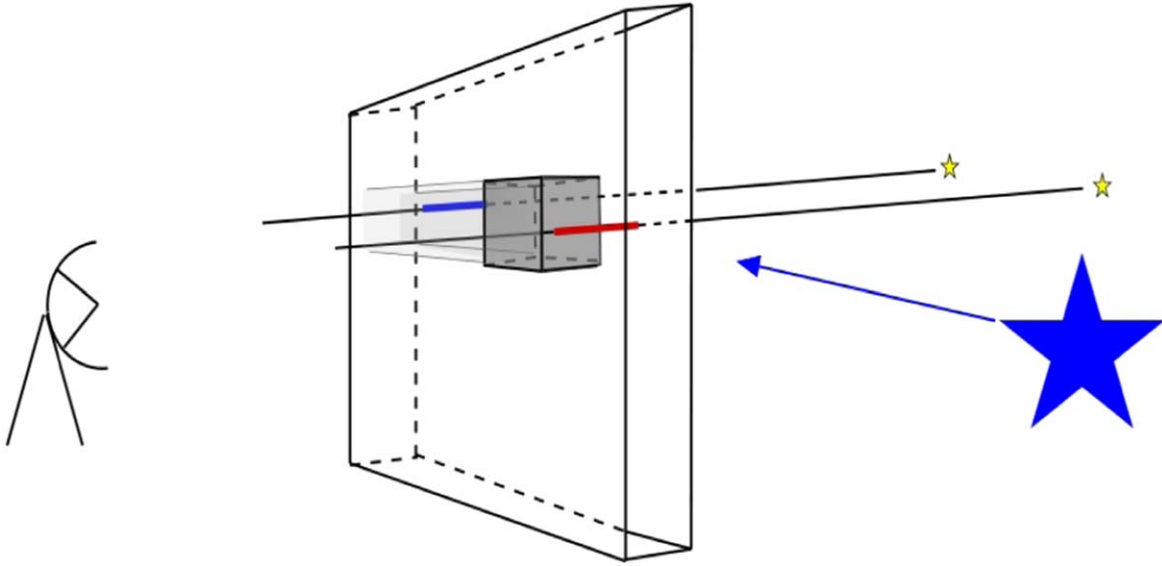


Figure 4. A sketch illustrating the structure of a clumpy cloud with an assumed slab geometry, illuminated by a bright, nearby star (γ Cas/ blue star), and probed by the lines of sight to distant (yellow) background stars. A dense clump in the cloud (shaded cuboid) will cast a shadow on the far side of γ Cas (light gray region). The gas on a line of sight in front of the clump (red line-segment) will therefore receive a higher radiation dose than gas on a line of sight in the shaded region (blue line-segment).

“third parameter” in these data (where RAT alignment and H_2 enhanced alignment are the first two).

The most prominent outliers in the plots (here and in Andersson et al. 2013) seem to be associated with large column density regions in the mm-wave maps, especially the compression ridge region at the side of the nebula facing γ Cas. If the column density can be used as a proxy for space density (i.e., if the cloud can to first order be approximated with a slab geometry) this is where the collision rate would be especially large. We therefore probe the hypothesis that the outliers represent enhanced collisional disalignment in the material.

4.2. Grain–Gas Collisions and Two Temperatures in IC 63

To probe for a dependence of the measured polarization on the collision rate, we assume that the direct radiative alignment rate of the grains in IC 63 is close to constant. This is supported by the fact that the opacity in the gas to photons capable of direct RAT alignment is relatively low as these are only constrained to have $\lambda < 2a$ (the opacity to H_2 dissociating photons is much smaller than the cloud size since they are much harder with $\lambda < 1108 \text{ \AA}$). We then find a nominal correlation with the H_2 fluorescent flux to account for the H_2 formation enhancement (as done in Andersson et al. 2013; Hoang et al. 2015). Based on this nominal P versus $I(\text{H}_2)$ relation we can investigate the possible role of collisions by comparing the deviations from this relationship (ΔP) with the integrated intensity of the HCO^+ line (W_{HCO^+}). We use the HCO^+ column density rather than visual extinction as it has higher accuracy and is assured to probe the IC 63 cloud only, rather than possible background gas. Other gas tracers, such as CO ($J = 1-0$) or its isotopomers might have been preferable, but are not available at the spatial resolution required to match the pencil beams of the polarimetry.

The result is shown in Figure 6. The overall distribution of points shows a weak anticorrelation (with a $\sim 45\%$ probability based on a *Spearman rank-order* test). However, a bifurcation

in the points is also evident. To explore this dichotomy, we plot the locations of the polarization lines of sight on a heavily stretched map of HCO^+ (Figure 3). This map allows us to separate the lines of sight into those that pass through IC 63 in front of, or behind, a dense clump in the cloud. We have marked the former with red symbols in both Figures 3 and 6 and the latter with blue symbols. A number of lines of sight do not clearly fall in either category and are plotted as white symbols in Figure 3. If the distinguishing separations between the different lines of sight is the illumination of the gas (and dust) by γ Cas, then these latter points shown with white color should be more closely related to the ones in front of a clump (red symbols), as the distinguishing characteristic is whether the radiation from the background star has been damped or not by the dense gas.

Considering the color scheme in Figure 3, we notice a clear separation of the full sample into two populations. The population with blue symbols which are in the shaded region behind HCO^+ clumps (Figure 3), show significantly shallower slope (-0.99 ± 0.06) than that of the population with the red symbols (-2.18 ± 0.46) which are in front of the HCO^+ clumps (see Figure 6). The two slopes here suggest different rates of drop in amount of polarization with the gas density.

The anticorrelation seen in the distribution is expected for the collisional disalignment, whose rate (C) is proportional to the gas density (n_{gas}) and gas velocity (v_{gas})

$$C \propto n_{\text{gas}} \cdot \sqrt{T_{\text{gas}}} \quad (5)$$

where, for thermal motion, the gas temperature (T_{gas}) is related to average velocity of the gas (v_{gas}) by relation $T_{\text{gas}} = \frac{\mu m_{\text{H}}}{k_B} v_{\text{gas}}^2$. As discussed above, we are here applying the local density variations in a perturbation mode around the steady-state solution described by Equation (4), which means that ΔP versus n_{gas} should show linear anticorrelation with a slope proportional to the square root of the gas temperature. If we, as suggested above, approximate the cloud as a slab geometry, then the integrated HCO^+ intensity can be used as a proxy for

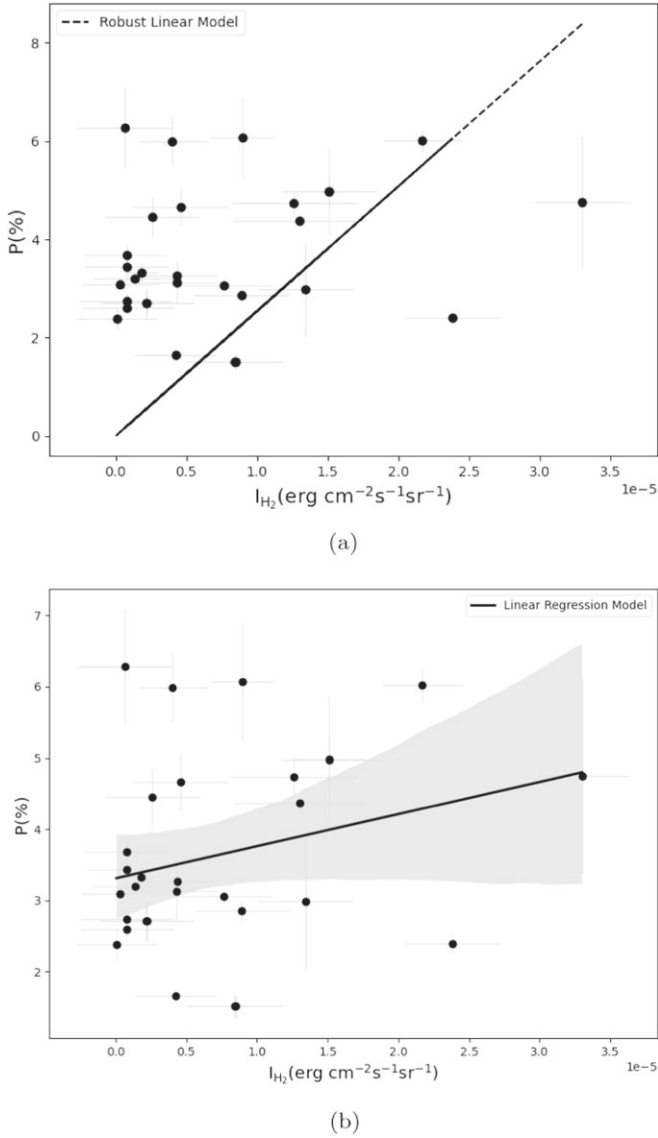


Figure 5. (a) Distribution of amount of polarization and diffused H_2 fluorescence with robust linear model fitting. (b) Smoother representation of P and H_2 fluorescence distributions using kernel density estimator (KDE).

gas density. Figure 6 shows two separate slopes fit to the two populations of targets shown in red and blue symbols with the point tracing more intensely illuminated gas following a steeper plot in ΔP versus W_{HCO^+} . This would be expected if the gas is heated by the radiation from the star and gas *in the shade* is cooler than the gas in the direct illumination of γ Cas radiation. Similar to the opacity differences between H_2 photodissociation and the subsequent re-formation, the photons responsible for heating the gas, through photoelectric emission from small grains will likely also have a higher effective opacity into the cloud than those responsible for the direct RAT alignment. This assumes that the small grain population is present in both “hot” and “cool” gas, which is likely as the clumps are not dense or dark enough to support significant grain growth (Ysard et al. 2013; Vaillancourt et al. 2020). This depends on the poorly known work function of the grain material, but if we assume a work function of 4.4 eV (equivalent to a photon wavelength of $\lambda = 2820$ Å) for graphite (PAHs) and 8 eV ($\Leftrightarrow \lambda = 1550$ Å)

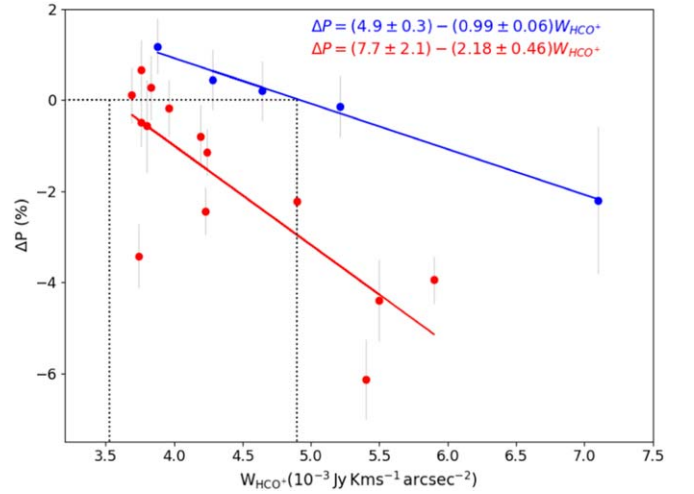


Figure 6. Variation of change in polarization fraction with HCO^+ integrated flux in the lines of sight corresponding to the stars shown in Figure 3. The color scheme used for targets in both the plots are consistent. The black dotted lines are $\Delta P = 0$ lines corresponding to critical densities of W_{HCO^+} (see text for explanation).

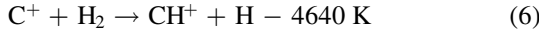
for silicates (Weingartner & Draine 2001), then also the gas heating is likely to be more spatially structured than the direct RAT alignment, and it is reasonable to thence separate the alignment from the disalignment dependence of the radiation field.

To probe the [dis]-alignment efficiency, the ideal probe would be the normalized fractional polarization (P/A_V), which removes changes due to total column density. However, while we have some A_V measurements of the targets shown in Figure 6 some line of sight extinction measurements are fully missing, while for others the existing ones are of marginal accuracy. Therefore, performing the analysis in P/A_V introduces additional uncertainties. Doing this analysis shows that the parameters of the two slopes in this figure are within the mutual uncertainties of those utilizing the normalized fractional polarization P/A_V , and implies that the approximation of the cloud as a plane-parallel slab is reasonable.

The two slopes in Figure 6 are consistent with the two-temperature hypothesis of Thi et al. (2009). The ratio of the square roots of the two temperatures 106 K and 685 K of warm and hot regions, respectively, in Figure 2 is 2.54 ± 1.83 . The ratio of the two slopes obtained in Figure 6 is 2.20 ± 0.49 . These values are consistent within their joint uncertainty of ~ 1.89 . The higher rate of gas–grain collision in the hot regions leads to higher disalignment rate of the aligned dust grains and hence stronger decrements in polarization, as seen in Figure 6.

The steady-state solution of the alignment (Equation (4)) has a $1/(n_{\text{gas}} \cdot \sqrt{T_{\text{gas}}})$ dependence in the RAT term, and, therefore, the $\Delta P = 0$ location should depend on these parameters. Figure 6 shows dotted lines plotted for $\Delta P = 0$ and the corresponding two integrated intensities of HCO^+ on the x-axis. This “critical density” for the hotter gas (toward higher temperature) occurs at a lower value than for the colder gas as would be expected from the above dependence. This supports our conclusion that the two sub-sets and their associated linear anticorrelations represent the two—warm and hot—phases of the gas in IC 63 PDR. It is possible to an unknown degree that the rotational disruption by RAT (RATD; Hoang et al. 2019) may play a minor role in affecting the critical density.

It is worth noting that a dual temperature distribution in the molecular hydrogen line excitation is a well known phenomenon in UV observations of diffuse gas. There, the $J = 1$, $J = 0$ excitation shows a temperature of typically ~ 80 – 130 K (Naslim et al. 2015) consistent with the cool neutral medium. For $J = 3$ and higher, a typically much higher excitation temperature is derived ~ 500 – 1000 K (Shaw et al. 2005). As shown by Lambert et al. (1990), the column density in the high J -levels is correlated with that of CH^+ . Since the formation path of this radical requires an endothermic reaction with an activation energy exceeding 4600 K:



(Pineau des Forets et al. 1986, and references therein), this implies that some gas along the line of sight either is now in warm/hot regions or recently was. Hence the two-temperature excitation seen in UV observations likely corresponds to distinct thermal components along the line of sight. Our proposed separation of thermal components corresponds to a similar structure, albeit in the plane of the sky.

5. Summary and Conclusions


We have combined optical polarization observations with H_2 and HCO^+ line observations toward the IC 63 cloud in order to investigate the effects on grain alignment efficiency and polarization values due to gas–grain collisions. We find that, assuming a close to constant direct radiative alignment rate (as suggested by Hoang et al. 2015) enhanced by H_2 formation torques, the polarization is decreased by gas–grain collisions consistent with a two-temperature structure, where the higher temperature corresponds to line-of-sight probing gas illuminated by the unattenuated radiation from γ Cas, and the lower temperature corresponds to gas shaded by dense clumps in the cloud. The ratio of the two slopes is consistent with the two-temperature solution seen in pure rotational excitation observations of H_2 (Thi et al. 2009). We find that the relative critical gas density at which the gas–grain collisions are sufficiently effective to disalign the grains is smaller in the hot gas than in the warm gas, supporting our conclusion. Further observations, including direct measurements of the gas space density, are required to confirm these conclusions.

We thank the anonymous referee for helping us to considerably improve the content of the paper. We gratefully acknowledge the generous telescope allocations by the review committees of the NOT and CFHT and the expert support by the observatory staff. The data set presented here was obtained in part using the Nordic Optical Telescope (NOT) with ALFOSC, which is provided by the Instituto de Astrofísica de Andalucía (IAA) under a joint agreement with the University of Copenhagen and NOTSA. Based also, in part, on observations obtained with WIRCAM, a joint project of the Canada–France–Hawaii Telescope (CFHT), Taiwan, Korea, Canada, France. The CFHT is operated by the National Research Council (NRC) of Canada, the Institut National des Sciences de l’Univers of the Centre National de la Recherche Scientifique of France, and the University of Hawaii. B.-G.A. and A.S. acknowledge financial support from the NSF through grant AST-1715876. J.E.V. acknowledges financial support from NASA through award # SOF 05-0038 issued by USRA. We thank Adam Mantz and Maria Jose Maureira for CARMA observations.

Facilities: CFHT, CARMA, WHT, AIMPOL, IRAM, NOT.

Software: Astropy (Astropy Collaboration et al. 2013), Matplotlib (Hunter 2007), SciPy (Virtanen et al. 2020), NumPy (Harris et al. 2020).

ORCID iDs

Archana Soam  <https://orcid.org/0000-0002-6386-2906>
 B.-G. Andersson  <https://orcid.org/0000-0001-6717-0686>
 Jose Acosta-Pulido  <https://orcid.org/0000-0002-0433-9656>
 Manuel Fernández López  <https://orcid.org/0000-0001-5811-0454>
 John E. Vaillancourt  <https://orcid.org/0000-0001-8916-1828>
 Vilppu Piirola  <https://orcid.org/0000-0003-0186-206X>
 Michael S. Gordon  <https://orcid.org/0000-0002-1913-2682>

References

- Andersson, B. G., Lazarian, A., & Vaillancourt, J. E. 2015, *A&A*, **53**, 501
 Andersson, B. G., Piirola, V., De Buizer, J., et al. 2013, *ApJ*, **775**, 84
 Andersson, B. G., Pintado, O., Potter, S. B., Straižys, V., & Charcos-Llorens, M. 2011, *A&A*, **534**, A19
 Andersson, B. G., & Potter, S. B. 2007, *ApJ*, **665**, 369
 Andersson, B. G., & Potter, S. B. 2010, *ApJ*, **720**, 1045
 Andrews, H., Peeters, E., Tielens, A. G. G. M., & Okada, Y. 2018, *A&A*, **619**, A170
 Astropy Collaboration, Robitaille, T. P., Tollerud, E. J., et al. 2013, *A&A*, **558**, A33
 Bradley, L., Sipőcz, B., Robitaille, T., et al. 2019, *astropy/photutils*: v0.6, Zenodo, doi:[10.5281/zenodo.2533376](https://doi.org/10.5281/zenodo.2533376)
 Caputo, M., Dennis, R., Andersson, B.-G., et al. 2021, *ApJ*, in press
 Chandrasekhar, S., & Fermi, E. 1953, *ApJ*, **118**, 113
 Crutcher, R. M. 2004, *Ap&SS*, **292**, 225
 Davis, L. 1951, *PhRv*, **81**, 890
 Davis, L. J., & Greenstein, J. L. 1951, *ApJ*, **114**, 206
 Dolginov, A. Z., & Mitrofanov, I. G. 1976, *Ap&SS*, **43**, 291
 Draine, B. T., & Lazarian, A. 1998, *ApJ*, **508**, 157
 Draine, B. T., & Weingartner, J. C. 1996, *ApJ*, **470**, 551
 Federman, S. R., Glassgold, A. E., & Kwan, J. 1979, *ApJ*, **227**, 466
 Fleming, B., France, K., Lupu, R. E., & McCandliss, S. R. 2010, *ApJ*, **725**, 159
 France, K., Andersson, B. G., McCandliss, S. R., & Feldman, P. D. 2005, *ApJ*, **628**, 750
 Harris, C. R., Millman, K. J., van der Walt, S. J., et al. 2020, *Natur*, **585**, 357
 Hoang, T., Lazarian, A., & Andersson, B. G. 2015, *MNRAS*, **448**, 1178
 Hoang, T., Tram, L. N., Lee, H., & Ahn, S.-H. 2019, *NatAs*, **3**, 766
 Hough, J. H., Aitken, D. K., Whittet, D. C. B., Adamson, A. J., & Chrysostomou, A. 2008, *MNRAS*, **387**, 797
 Hunter, J. D. 2007, *CSE*, **9**, 90
 Jansen, D. J., van Dishoeck, E. F., & Black, J. H. 1994, *A&A*, **282**, 605
 Jansen, D. J., van Dishoeck, E. F., Black, J. H., Spaans, M., & Sosin, C. 1995, *A&A*, **302**, 223
 Jones, R. V., & Spitzer, L. J. 1967, *ApJ*, **147**, 943
 Jones, T. J., Hyland, A. R., & Bailey, J. 1984, *ApJ*, **282**, 675
 Karr, J. L., Noriega-Crespo, A., & Martin, P. G. 2005, *AJ*, **129**, 954
 Kaufman, M. J., Wolfire, M. G., Hollenbach, D. J., & Luhman, M. L. 1999, *ApJ*, **527**, 795
 Lambert, D. L., Sheffer, Y., & Crane, P. 1990, *ApJL*, **359**, L19
 Lazarian, A., & Draine, B. T. 1997, *ApJ*, **487**, 248
 Lazarian, A., & Draine, B. T. 1999, *ApJL*, **520**, L67
 Lazarian, A., & Hoang, T. 2007, *MNRAS*, **378**, 910
 Lazarian, A., & Roberge, W. G. 1997, *ApJ*, **484**, 230
 Mathis, J. S. 1986, *ApJ*, **308**, 281
 Medan, I., & Andersson, B.-G. 2019, *ApJ*, **873**, 87
 Morata, O., & Herbst, E. 2008, *MNRAS*, **390**, 1549
 Naslim, N., Kemper, F., Madden, S. C., et al. 2015, *MNRAS*, **446**, 2490
 Pineau des Forets, G., Flower, D. R., Hartquist, T. W., & Dalgarno, A. 1986, *MNRAS*, **220**, 801
 Polehampton, E. T., Wyrowski, F., & Schilke, P. 2005, in *IAU Symp.* 231, *Astrochemistry: Recent Successes and Current Challenges*, ed. D. C. Lis, G. A. Blake, & E. Herbst (Cambridge: Cambridge Univ. Press), 148
 Puget, P., Stadler, E., Doyon, R., et al. 2004, *Proc. SPIE*, **5492**, 978
 Purcell, E. M. 1979, *ApJ*, **231**, 404

- Röllig, M., Abel, N. P., Bell, T., et al. 2007, [A&A](#), **467**, 187
- Sault, R. J., & Noordam, J. E. 1995, [A&As](#), **109**, 593
- Shaw, G., Ferland, G. J., Abel, N. P., Stancil, P. C., & van Hoof, P. A. M. 2005, [ApJ](#), **624**, 794
- Soam, A., Andersson, B.-G., Straizys, V., et al. 2021, *AJ*, submitted
- Soam, A., Maheswar, G., Lee, C. W., Neha, S., & Andersson, B. G. 2017, [MNRAS](#), **465**, 559
- Stecher, T. P., & Williams, D. A. 1967, [ApJL](#), **149**, L29
- Thi, W. F., van Dishoeck, E. F., Bell, T., Viti, S., & Black, J. 2009, [MNRAS](#), **400**, 622
- Thi, W. F., van Dishoeck, E. F., Jansen, D. J., et al. 1997, in *The First ISO Workshop on Analytical Spectroscopy*, ESA SP-419, ed. A. M. Heras et al. (Noordwijk: ESA), 299
- Tielens, A. G. G. M. 2005, *The Physics and Chemistry of the Interstellar Medium* (Cambridge: Cambridge Univ. Press)
- Troland, T. H., & Crutcher, R. M. 2008, [ApJ](#), **680**, 457
- Vaillancourt, J. E., Andersson, B.-G., Clemens, D. P., et al. 2020, [ApJ](#), **905**, 157
- van Dishoeck, E. F., & Black, J. H. 1986, [ApJS](#), **62**, 109
- van Leeuwen, F. 2007, [A&A](#), **474**, 653
- Virtanen, P., Gommers, R., Oliphant, T. E., et al. 2020, [NatMe](#), **17**, 261
- Weingartner, J. C., & Draine, B. T. 2001, [ApJS](#), **134**, 263
- Whittet, D. C. B. 2003, *Dust in the Galactic Environment* (2nd ed.; Bristol: IOP Publishing), 390
- Whittet, D. C. B., Hough, J. H., Lazarian, A., & Hoang, T. 2008, [ApJ](#), **674**, 304
- Ysard, N., Abergel, A., Ristorcelli, I., et al. 2013, [A&A](#), **559**, A133